Anisotropic thermal conductivity in the polycrystalline environmental barrier coating β-$Y_2Si_2O_7$

David H. Olson,[1] Valentina A. Avincola,[2] Cory G. Parker,[2] Jeffrey L. Braun,[1] John T. Gaskins,[1] Elizabeth J. Opila,[2] and Patrick E. Hopkins[1,2,3,a)]

[1)]*Department of Mechanical and Aerospace Engineering, University of Virginia, Charlottesville, VA 22904, USA*

[2)]*Department of Materials Science and Engineering, University of Virginia, Charlottesville, VA 22904, USA*

[3)]*Department of Physics, University of Virginia, Charlottesville, VA 22904, USA*

We experimentally investigate the anisotropic thermal conductivity in beta-phase yttrium disilicate (β-$Y_2Si_2O_7$). This is achieved through a combined frequency- and time-domain thermoreflectance mapping technique correlated to scanning electron and electron-backscatter diffraction micrographs. Doing so allows us to examine the thermal conductivity of various grains of different orientations, ultimately allowing for the determination of the thermal conductivity tensor of the system. β-$Y_2Si_2O_7$ shows strong anisotropy in its thermal conductivity, with a 25% change in thermal conductivity from the most to least insulating orientation.

Aerospace applications necessitate the use of unique materials to withstand extreme environments. The need for environmental barrier coatings (EBCs) are of particular importance in limiting the oxidation of aerospace components and the volatility of the SiO_2 scale commonly found in silicon-based ceramic matrix composites. Materials possessing high water-vapor resistance, have low thermal expansion coefficients, and chemical and mechanical stability at high temperatures are particularly attractive for EBC applications.[1] Specifically, rare earth (RE) silicates have been shown to exhibit the above qualities,[2,3] with the capacity to withstand temperatures up to 1316 ° C for thousands of hours.[4] These combined characteristics have brought RE silicates to the forefront of technological relevance in the search for EBCs for future gas turbine engine applications.

Yttria-based disilicates ($Y_2Si_2O_7$) have been identified as a candidate for EBCs, owing initially to their high melting temperature, in excess of 1500 ° C.[5] Additionally, γ- and β-$Y_2Si_2O_7$ posse a coefficient of thermal expansion comparable to that of SiC which offers relief from the stresses arising from thermal cycling.[2,6–11] In spite of the potential issues with oxidation resistance and subsequent material recession, $Y_2Si_2O_7$ continues to offer promise as a candidate system for EBC applications.

The thermal conductivity associated with these disilicates is an additional property that needs to be taken into consideration when designing EBCs. Despite its importance, a robust analysis of the thermal conductivity of these materials has not been performed to date. Various works have examined the thermal conductivity of yttria-based silicates in their bulk form with values ranging from 0.161 to 4.91 Wm^{-1} K^{-1}, depending on the porosity of the system.[10–14] Thermal conductivity for these reported values representing generally represent an average thermal conductivity of a polycrystalline, possibly multi-phase system. For example, in all of the aforementioned reports of yttria-based silicate thermal conductivity, laser-flash was employed, thus sampling the average thermal diffusivity over the entire volume of the sample. These measurements cannot isolate the microstructural or anisotropic influences that different grains have on thermal transport in the sample.

Indeed, these influences have the potential to incite local fracture and ultimate failure in these EBCs. For example, Clarke *et al.*[12] have shown that at high temperatures, the thermal conductivity of various disilicates can achieve exceptionally low values, reaching the theoretical minimum limit to thermal conductivity,[15] whereby a phonon mean free path of one half of a period of oscillation of the vibrational energies is achieved. Additionally, they demonstrate that the thermal conductivity of Y-, Yb-, and Lu- based disilicates can theoretically be anisotropic. For these complicated systems, an anisotropic thermal conductivity tensor dictating the flow of heat is not to be ignored, and has the potential to largely influence EBC applications at the macroscale.

In this work, we experimentally measure the thermal conductivity tensor of β-$Y_2Si_2O_7$. This is achieved by employing a modulated laser-based pump-probe technique to probe length scales on the order of several microns. By locally probing grains and correlating their crystalline orientations to electron-backscatter diffraction (EBSD) data, we measure the orientation-dependence of heat conduction as quantified by the thermal conductivity. In doing so, we are able to determine the thermal conductivity tensor of the monoclinic system, β-$Y_2Si_2O_7$. We find that β-$Y_2Si_2O_7$ is anisotropic, showing a 25% change in thermal conductivity from the least to most insulating orientation. This strong variation in thermal conductivity of polycrystalline β-$Y_2Si_2O_7$ based on grain orientation, which is driven by the naturally large anisotropy in the system, has major implications in modeling EBCs from a continuum perspective, and predicting mechanisms of failure based on local thermal strains arising.

Typically, optical pump-probe techniques utilizing higher modulation frequencies are relatively insensitive to in-plane thermal conductivities compared to cross-plane thermal conductivities. At lower modulation frequencies, time- and frequency-domain thermoreflectance (TDTR and FDTR) can gain increased sensitivities to anisotropy in the thermal con-

[a)]phopkins@virginia.edu

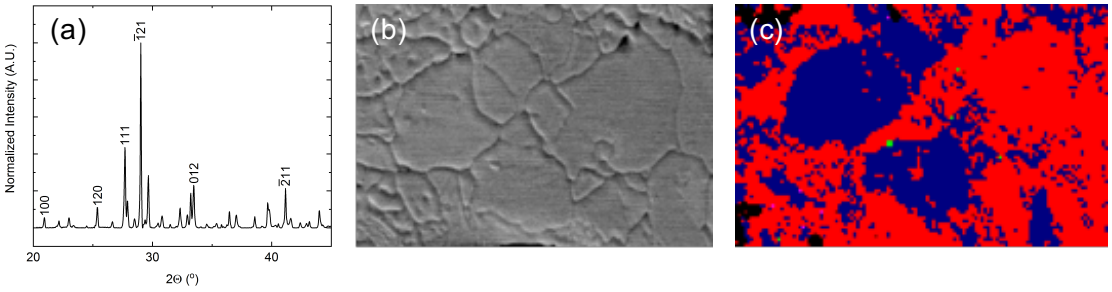

Figure 1. (a) X-ray diffractogram of the sample of interest, confirming the γ phase of the disilicate. The associated lattice parameters are a = 4.68824 Å, b = 10.84072 Å, c = 5.58219 Å, and β = 96.0325°, consistent with those found in the literature. (b) Representative SEM of select grains for reference. (c) Phase identification via EBSD. The regions in red and blue are the β and γ phases, respectively, of $Y_2Si_2O_7$. We take the lattice parameters of β-$Y_2Si_2O_7$ to be a = 6.869 Å, b = 8.960 Å, c = 4.717 Å, and β = 101.73°.

ductivity tensor. Various methods have been proposed for the measurement of the anisotropy, including beam-offset[16–18] and elliptic beam techniques.[19,20] While versatile, these methods are highly sensitive to the ellipticity of the beam and the repeatability of the measured FWHM of the cross-correlation of the pump and probe in beam-offset approaches.[17]. Recently, several works have employed FDTR and TDTR thermal conductivity mapping techniques,[21–26] whereby the thermal properties of a given sample can be spatially mapped on the order of several microns to extract properties of interest. Indeed, Yang *et al.*[25] have shown that the spatially varying anisotropic thermal conductivity of few layer graphene can be extracted via this technique. The ability to map the spatial anisotropy of thermal conductivity, and relate this spatial distribution of thermal transport to the local variation in crystal structure and phase in materials, would provide a foundational advance in our understanding of nanoscale heat transport properties of composite materials. More specifically, local variations in thermal conductivity driven by crystalline anisotropy, and the spatial distribution of these variations, will provide a link between the nano/microscale and the bulk/average thermal conductivity of polycrystalline and other structurally heterogeneous materials. These measurements have implications on a wide array of material technologies, focusing here on EBCs where local variations in temperature and resultant hot spots may lead to thermomechanical failure.

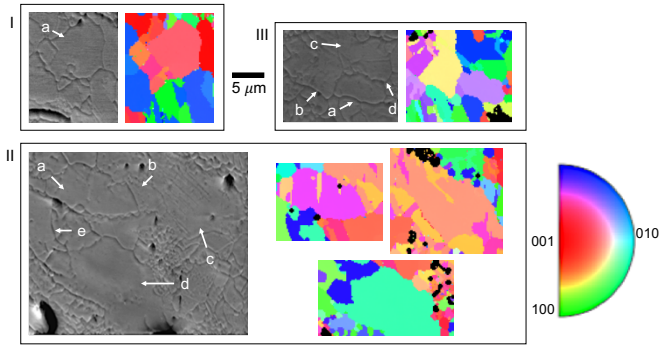

Figure 2. SEM and EBSD micrographs of the grains of interest. Regions are denoted by roman numerals in the top left of each box, while grains of each region are shown in white and denoted alphabetically. The pole figure demonstrates orientation of the grains in EBSD micrographs. Note that all EBSD micrographs contain grains with those of similar and different orientations, suggesting the ability to recreate the thermal conductivity tensor of the system.

To determine the anisotropic thermal conductivity of β-$Y_2Si_2O_7$, we fabricate $Y_2Si_2O_7$ via an air plasma spray (APS) deposition, the details of which can be found in the Supplementary Information. A post-anneal of 1200 °C for 24 hours in ambient conditions was performed in order to finalize the heterogeneous mixture of the system. The post-annealed sample obtained is polycrystalline with microstructural features on the order of tens of microns. Representative x-ray diffraction (XRD) of the sample can be seen in Fig. 1(a), which shows that the sample is primarily of the γ phase of $Y_2Si_2O_7$, based on similar lattice parameters found in the literature[9]. Shown in Figs. 1(b) and (c) are representative SEM and EBSD micrographs of select grains. The phase image indicates that both γ- and β-$Y_2Si_2O_7$ are present in our sample. The appearance of additional phases via EBSD is not uncommon, as the region averaged over in a XRD measurement is much larger than that of EBSD. Because of the predominantly β phase in our EBSD maps, we choose to analyze anisotropic thermal conductivity solely in this phase. EBSD phase micrographs for additional regions analyzed in this work are entirely of the β phase. We further selectively examine areas via ESBD to verify crystalline orientations of various grains in different regions of the sample. Grains of interest can be seen in representative EBSD and SEM micrographs in Fig. 2. We note that various orientations of the disilicate are present, with grain sizes on the order of $\sim$5 μm. The specific lattice parameters of β-$Y_2Si_2O_7$ are a = 6.8691 Å, b = 8.960 Å, c = 4.7168 Å, and β = 101.73°, which are important for the analysis of the thermal conductivity tensor presented later. Grain identifiers and nearest atomic planes can be found in Table I. We identify each grain by region and alphabetic number (i.e., grain a

Region	Grain	Nearest Atomic Plane [$h\ k\ l$]	Thermal Conductivity (W m^{-1} K^{-1})
I	a	[$\bar{1}\bar{2}$ $\bar{9}\bar{0}$ 8]	6.5 ± 0.4
II	a	[81 $\bar{1}\bar{2}$ $\bar{7}\bar{2}$]	6.4 ± 0.5
	b	[$\bar{1}\bar{8}$ 9 $\bar{1}\bar{8}$]	5.5 ± 0.4
	c	[$\bar{1}\bar{2}$ $\bar{5}\bar{4}$ $\bar{4}\bar{8}$]	5.7 ± 0.5
	d	[$1\bar{0}\bar{8}$ $4\bar{0}\bar{8}$ $\bar{7}\bar{2}$]	5.7 ± 0.5
	e	[42 42 37]	6.2 ± 0.6
III	a	[$\bar{8}$ 12 8]	6.9 ± 0.5
	b	[45 70 63]	7.1 ± 0.4
	c	[5 3 0]	7.5 ± 0.4
	d	[$\bar{9}$ 8 0]	7.3 ± 0.5

Table I. Mapping region, grain identifier, nearest atomic plane, and derived thermal conductivities for each of the grains analyzed in this work.

in region I will be identified as grain Ia). We deposit an aluminum transducer with nominal thickness of 80 nm for the implementation of spatial thermal conductivity mapping via TDTR.

TDTR and similar pump-probe metrologies are widely discussed throughout the literature,[27–29] and will therefore not be discussed in depth here; specific details of our TDTR experiment can be found in the Supporting Information. A standard TDTR configuration interrogates a single point on the sample surface. While convenient for applications in which there are few surface inhomogeneities, understanding how thermal conductivity varies across a given samples surface can yield insight into the anisotropic or compositional effects on thermal conductivity. To better understand these effects, we mount our $Y_2Si_2O_7$ sample on a 3-axis stage, with motors along the sample orientation having a bidirectional repeatability of $<$1.5 μm and a closed-loop piezo motor controlling the focal plane of the sample. We orient the stage in such a way such that movements along the sample surface result in no appreciable change in focus. An appropriate time delay is chosen, defined further below, and the sample is rastered over a region of interest to probe the thermal conductivity as a function of microstructural variation across the sample.

Using a typical thermal model for a two layer system (i.e., 80 nm Al transducer on a substrate), TDTR is capable of measuring both the thermal boundary conductance between the Al transducer and the underlying disilicate, as well as the thermal conductivity of the disilicate. To perform thermal conductivity mapping, however, the thermal boundary conductance should be adequately known, as the data from a single pump-probe delay time is used to extract the thermal conductivity of the underlying material. We take numerous full TDTR scans across all regions of interest and fit for the thermal conductivity of the disilicate and the thermal boundary conductance between the disilicate and the underlying material. At a modulation frequency of 8.4 MHz, we maintain one-dimensionality and are sensitive to primarily the cross-plane thermal conductivity and thermal boundary conductance, leaving any influence from in-plane transport to be negligible. We find that the thermal boundary conductance across all grains to be $\sim 40 \pm 10$ MW m^{-2} K^{-1}, and use this value for the determination of our pump-probe delay time for the mapping procedure. The sensitivity to the thermal boundary conductance is minimized at a given time delay for each conductance, and this is the pump-probe delay time at which we take subsequent measurements. For regions I, II, and III, we choose pump-probe delay times of 3360, 1360, and 1920 ps. The RMS pump/probe radii in our measurements is ~ 6.4 μm, and is determined by fitting the spot size using a sapphire reference sample.

Thermal conductivity maps of the three regions of interest can be seen in Fig. 3, alongside the reflected probe auxiliary signal, which is subtracted from the reference beam in our balanced photodetector scheme. The auxiliary signal is indicative of pixels in which the probe beam is not specularly reflected, and therefore cannot be adequately interpreted. Monitoring this signal also allows us to more readily identify grains in each of the three regions. In our analysis, we select regions in which the subtracted auxiliary signal does not exceed 0.03 V so as to not be heavily influenced by diffusely scattered light. We do not expect a reduction in the thermal conductivity near grain boundaries to influence our results, as this is only to be expected in materials with thermal conductivities on the order of diamond.[26] In all maps, we find that the thermal conductivity distributions vary about ~ 6 W m^{-1} K^{-1}.

Tabulated values of thermal conductivities for all grains analyzed can be found in Table I. The stereographic projection

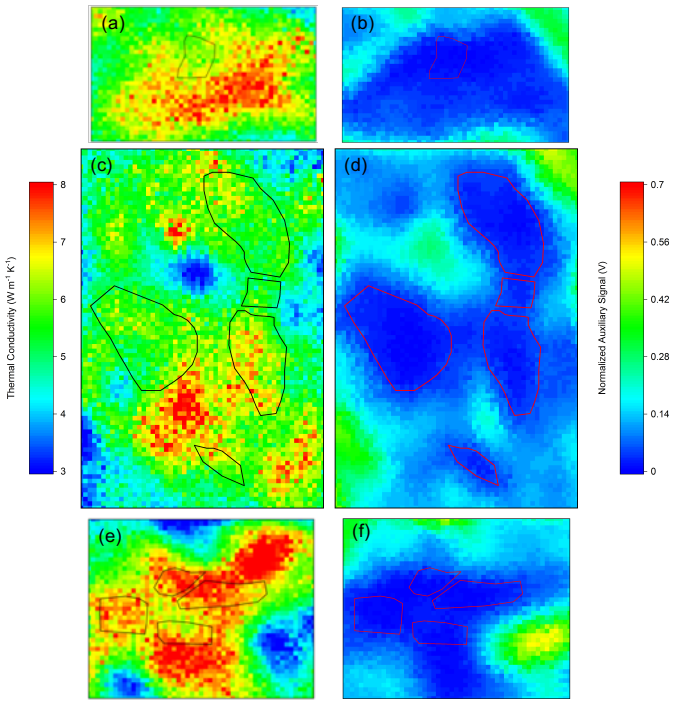

Figure 3. Thermal conductivity maps (a,c,e) and normalized auxiliary signals (b,d,f) of probed regions. Regions outlined in black on the thermal conductivity maps and red in the normalized auxiliary signals are regions chosen to be analyzed based on the grains identified in Fig. 2.

of the measured values with respect to the monoclinic system can be found in Fig. 4(a), where the labeled values include the measured thermal conductivity and their uncertainty. The thermal conductivity of β-$Y_2Si_2O_7$ ranges from 5.5 to 7.5 W m^{-1} K^{-1}, showing anisotropy in the thermal conductivity of the system. We further examine the thermal conductivity from a continuum approach, extracting the thermal conductivity tensor of the system. The thermal conductivity tensor of a monoclinic system takes the form[30]

$$\widetilde{\mathbf{K}} = \begin{bmatrix} \kappa_{xx} & 0 & \kappa_{xz} \\ 0 & \kappa_{yy} & 0 \\ \kappa_{zx} & 0 & \kappa_{zz} \end{bmatrix},$$

where κ_{xx} and κ_{yy} are thermal conductivities measured along the [100] and [010] directions, respectively, and κ_{zz} is the thermal conductivity measured along the orthogonal to [100] and [010], β-90 degrees from the [001] direction, where β is the angle between the [100] and [001] directions. We will refer to the [100] and [010] directions as $\hat{x}$ and $\hat{y}$, respectively, and the orthogonal to the two as $\hat{z}$. One can explicitly derive the angular dependence of thermal conductivity of a monoclinic system on θ and ϕ:

$$\kappa(\theta,\phi) = \kappa_{xx}\sin^2\phi\cos^2\theta + \kappa_{yy}\sin^2\phi\sin^2\theta + \kappa_{zz}\cos^2\phi + 2\kappa_{xz}\sin\phi\cos\theta\cos\phi. \quad (1)$$

In this equation, ϕ is the angle from the $\hat{z}$ direction, and θ is the angle from the $\hat{x}$ direction to the projection of the grain orientation onto the $\hat{x}$-$\hat{y}$ plane.

Of all the grains presented in Table I, we perform a least-squares minimization of Eq. 1 to extract the necessary components of the thermal conductivity tensor. In all, we find that the thermal conductivity tensor takes the form:

$$\widetilde{\mathbf{K}} = \begin{bmatrix} 7.5 & 0 & -0.5 \\ 0 & 6.1 & 0 \\ -0.5 & 0 & 6.1 \end{bmatrix} \text{ W m}^{-1}\text{ K}^{-1}.$$

It is interesting to note that the off-axis term in the tensor, κ_{xz}, retains a negative thermal conductivity value. We would like to iterate the fact that the appearance of this term is due to the deflection of the monoclinic system from the Cartesian coordinate system, and that the determinant of the thermal conductivity tensor must be positive so as to be in congruence with the second law of thermodynamics. The negative thermal conductivity of κ_{xz} suggests that a temperature gradient imposed in the $\hat{x}$ direction would result in a heat flux in the -$\hat{z}$ direction, and vice versa. Similar results have been procured for monoclinic β-Ga_2O_3.[31]

To better visualize the thermal conductivity tensor of this system as it relates to the structure, we plot these thermal conductivities as a stereographic projection of the crystal system, shown in Fig. 4(b). We note that the thermal conductivity along the [100] and [$\bar{1}$00] directions are identical in thermal conductivity due to the symmetry of the monoclinic system. We also find that the thermal conductivity along the [001] direction is similar to that of the [010] direction, and that they are both smaller in magnitude than the [100] direction. The maximum attainable thermal conductivity occurs between the [1–] and [$\bar{1}$00] directions.

From the kinetic theory of gasses, the phonon contribution to thermal conductivity can be approximated as $\kappa = \frac{1}{3}Cv\lambda$[32]. In this equation, C is the volumetric heat capacity, v is the group velocity of thermal carriers, and λ is the phonon mean free path. We take C to be identical for each of the crystalline orientations, which is plausible because size effects on heat capacity do not present themselves until the dimensions of the system approach the phonon wavevector, and λ to be the same for each crystalline orientation as we do not expect scattering mechanisms to preferentially adhere to a single crystal orientation. Under these assumptions, the primary factor regarding the measured changes in thermal conductivity must be attributed to changes in phonon group velocity. In most crystals, low-frequency phonon modes primarily govern the transmission of heat, and thus the group velocity can roughly be approximated as the speed of sound. In a simplistic approach, $v \propto \sqrt{Y}$, where Y is the Young's modulus.[33] As the a and c lattice parameters are smaller than that of b, one would expect the Young's modulus in these directions to be larger, as the overall bond is shorter, and therefore stronger. This realizes the higher thermal conductivity along the [100] and [010] directions, while a lower thermal conductivity is found in the [001] direction. Jiang *et al.* have found similar results in β-Ga_2O_3,[31], and the correlation between modulus and thermal conductivity are well documented in the literature.

Very few works in the literature have experimentally ex-

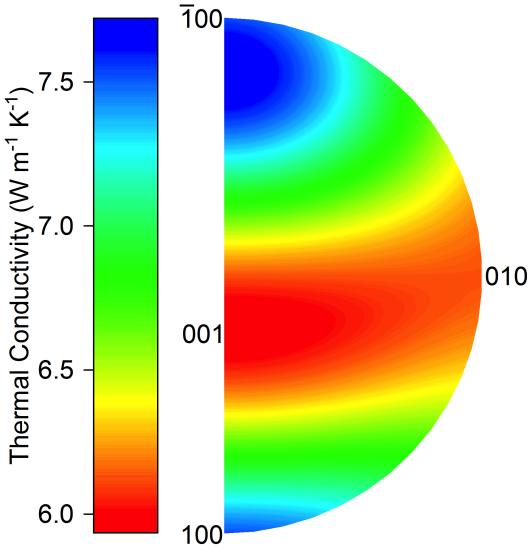

Figure 4. The thermal conductivity of β-$Y_2Si_2O_7$ represented as a stereographic projection of the monoclinic system.

amined the anisotropic thermal conductivity of β-$Y_2Si_2O_7$. Zhou *et al.*[34] and Tian *et al.*[35] both presented experimental measurements of thermal diffusivity via the laser-flash method. In both previous works, heat capacity was confirmed independently, either by differential scanning calorimetry (DSC) or by employing the Neumann-Kopp rule as an approximation based on the constituents of the system. Regardless, both previous works describe the thermal conductivity of a bulk system, where microstructural effects and anisotropy are averaged to determine single thermal conductivity. To that point, Tian *et al.*[35] have determined the anisotropic minimum thermal conductivity based on the Debye approximation in the high-temperature limit, showing a two-fold change in thermal conductivity based on crystalline orientation. However, in their work, they assume that the phonon group velocity can be extracted from an anisotropic Young's modulus. In general, the thermal conductivity is related to the Young's modulus. However, the phase space in which the thermal conductivity tensor can occupy is that of an ellipsoid, with axes relating to the magnitude of the components of the thermal conductivity tensor. Because the elastic tensor is a rank 4 tensor, the phase space that it occupies is not that of an ellipsoid. Thus, the anisotropic claims made by Tian *et al.*[35] are invalidated. Our values are higher than those found in the literature for room temperature measurements; however, we can attribute the differences in our results to the measurement technique. For polycrystalline samples in laser flash techniques, an average thermal conductivity of all crystalline directions and polymorphs is determined. One can define an effective thermal conductivity related to the determinant of the tensor determined as $\kappa_{eff} = \sqrt[3]{\det(\widetilde{\mathbf{K}})}$, where the cube root arises due to the dimensionality of the system. For our results, we find that κ_{eff} = 6.5 W m^{-1} K^{-1}. Our results are the first to report on spatially monitoring thermal conductivity via TDTR to reproduce the thermal conductivity tensor of a material system, specifically that of β-$Y_2Si_2O_7$. One would expect a similar tensor for $Y_2Si_2O_7$ of the γ and ζ polymorphs, as they are also of a monoclinic structure.

In summary, we fabricated the EBC $Y_2Si_2O_7$ and find that it is polycrystalline, containing various polymorphs of the disilicate. Conventional methods of determining the thermal conductivity of these materials rely on bulk sample measurements, which do not yield insight into the microstructurally dependent thermal conductivity of individual grains, instead averaging the thermal conductivity of the entire system. We show that TDTR is capable of spatially separating thermal conductivities in grains on the order of ~ 5 μm. This allows us to verify anisotropy in the thermal conductivity of the disilicate based on EBSD-correlated grain orientation, ultimately providing us with the ability to calculate the thermal conductivity tensor of the system. In all, this work demonstrates the power of laser-based transient techniques for the determination of thermal conductivity for samples in which variations in thermal conductivity at the microstructural level are present in the material system.

D. H. Olson is grateful for funding from the National Defense Science and Engineering Graduate (NDSEG) and Virginia Space Grant Consortium (VSGC) Fellowships.

REFERENCES

[1] F. W. Zok, Ceramic-matrix composites enable revolutionary gains in turbine engine efficiency, American Ceramic Society Bulletin 95 (2016) 22–28.

[2] K. N. Lee, D. S. Fox, N. P. Bansal, Rare earth silicate environmental barrier coatings for SiC/SiC composites and Si_3N_4 ceramics, Journal of the European Ceramic Society 25 (2005) 1705–1715.

[3] Y. Xu, X. Hu, F. Xu, K. Li, Rare earth silicate environmental barrier coatings: Present status and prospective, Ceramics International 43 (2017) 5847–5855.

[4] H. E. Eaton, G. D. Linsey, K. L. More, J. B. Kimmel, J. R. Price, N. Miriyala, EBC Protection of SiC/SiC Composites in the Gas Turbine Combustion Environment, in: ASME Turbo Expo 2000: Power for Land, Sea, and Air, ASME, 2000, p. V004T02A018.

[5] N. A. Toropov, I. A. Bondar, Silicates of the rare earth elements, Bulletin of the Academy of Sciences of the USSR Division of Chemical Science 10 (1961) 502–508.

[6] M. Aparicio, A. Durán, Yttrium Silicate Coatings for Oxidation Protection of Carbon-Silicon Carbide Composites, Journal of the American Ceramic Society 83 (2004) 1351–1355.

[7] H. Klemm, Silicon Nitride for High-Temperature Applications, Journal of the American Ceramic Society 93 (2010) 1501–1522.

[8] K. Fukuda, H. Matsubara, Thermal Expansion of δ-Yttrium Disilicate, Journal of the American Ceramic Society 87 (2004) 89–92.

[9] M. D. Dolan, B. Harlan, J. S. White, M. Hall, S. T. Misture, S. C. Bancheri, B. Bewlay, Structures and anisotropic thermal expansion of the α, β, γ, and δ polymorphs of $Y_2Si_2O_7$, Powder Diffraction 23 (2008) 20–25.

[10] N. Al Nasiri, N. Patra, D. Horlait, D. D. Jayaseelan, W. E. Lee, Thermal Properties of Rare-Earth Monosilicates for EBC on Si-Based Ceramic Composites, Journal of the American Ceramic Society 99 (2015) 589–596.

[11] Z. Sun, Y. Zhou, J. Wang, M. Li, Thermal Properties and Thermal Shock Resistance of γ-$Y_2Si_2O_7$, Journal of the American Ceramic Society 91 (2008) 2623–2629.

[12] D. R. Clarke, Materials selection guidelines for low thermal conductivity thermal barrier coatings, Surface and Coatings Technology 163 (2003) 67–74.

[13] Z. Wu, L. Sun, P. Wan, J. Li, Z. Hu, J. Wang, In situ foam-gelcasting fabrication and properties of highly porous γ-$Y_2Si_2O_7$ ceramic with multiple pore structures, Scripta Materialia 103 (2015) 6–9.

[14] Z. Wu, L. Sun, P. Wan, J. Wang, Preparation, microstructure and high temperature performances of porous γ-Y 2 Si 2 O 7 by in situ foam-gelcasting using gelatin, Ceramics International 41 (2015) 14230–14238.

[15] D. G. Cahill, S. K. Watson, R. O. Pohl, Lower limit to the thermal conductivity of disordered crystals, Physical Review B 46 (1992) 6131–6140.

[16] J. P. Feser, D. G. Cahill, Probing anisotropic heat transport using time-domain thermoreflectance with offset laser spots, Review of Scientific Instruments 83 (2012) 104901.

[17] J. P. Feser, J. Liu, D. G. Cahill, Pump-probe measurements of the thermal conductivity tensor for materials lacking in-plane symmetry, Review of Scientific Instruments 85 (2014) 104903.

[18] D. Rodin, S. K. Yee, G. W. Woodruff, Simultaneous measurement of in-plane and through-plane thermal conductivity using beam-offset frequency domain thermoreflectance, Journal of Applied Physics 88 (2017) 14902.

[19] P. Jiang, X. Qian, R. Yang, Tutorial: Time-domain thermoreflectance (TDTR) for thermal property characterization of bulk and thin film materials, Journal of Applied Physics 124 (2018) 161103.

[20] M. Li, J. S. Kang, Y. Hu, Anisotropic thermal conductivity measurement using a new Asymmetric-Beam Time-Domain Thermoreflectance (AB-TDTR) method, Review of Scientific Instruments 89 (2018) 84901.

[21] X. Zheng, D. Cahill, P. Krasnochtchekov, R. Averback, J.-C. Zhao, High-throughput thermal conductivity measurements of nickel solid solutions and the applicability of the WiedemannFranz law, Acta Materialia 55 (2007) 5177–5185.

[22] J.-C. Zhao, X. Zheng, D. G. Cahill, High-throughput diffusion multiples, Materials Today 8 (2005) 28–37.

[23] E. López-Honorato, C. Chiritescu, P. Xiao, D. G. Cahill, G. Marsh, T. Abram, Thermal conductivity mapping of pyrolytic carbon and silicon carbide coatings on simulated fuel particles by time-domain thermoreflectance, Journal of Nuclear Materials 378 (2008) 35–39.

[24]C. Wei, X. Zheng, D. G. Cahill, J.-C. Zhao, Invited Article: Micron resolution spatially resolved measurement of heat capacity using dual-frequency time-domain thermoreflectance Simultaneous measurement of thermal conductivity and heat capacity of bulk and thin film materials using frequency-depend, Citation: Review of Scientific Instruments 84 (2013) 71301.

[25]J. Yang, E. Ziade, C. Maragliano, R. Crowder, X. Wang, M. Stefancich, M. Chiesa, A. K. Swan, A. J. Schmidt, Thermal conductance imaging of graphene contacts, Journal of Applied Physics 116 (2014) 023515.

[26]A. Sood, R. Cheaito, T. Bai, H. Kwon, Y. Wang, C. Li, L. Yates, T. Bougher, S. Graham, M. Asheghi, M. Goorsky, K. E. Goodson, Direct Visualization of Thermal Conductivity Suppression Due to Enhanced Phonon Scattering Near Individual Grain Boundaries, Nano Letters 18 (2018) 3466–3472.

[27]P. E. Hopkins, J. R. Serrano, L. M. Phinney, S. P. Kearney, T. W. Grasser, C. T. Harris, Criteria for cross-plane dominated thermal transport in multilayer thin film systems during modulated laser heating, Journal of Heat Transfer 132 (2010) 81302.

[28]A. J. Schmidt, X. Chen, G. Chen, Pulse accumulation, radial heat conduction, and anisotropic thermal conductivity in pump-probe transient thermoreflectance, Review of Scientific Instruments 79 (2008) 114902.

[29]D. G. Cahill, Analysis of heat flow in layered structures for time-domain thermoreflectance, Review of Scientific Instruments 75 (2004) 5119–5122.

[30]R. E. Newnham, Properties of Materials: Anisotropy, Symmetry, Structure, Oxford University Press USA - OSO, Oxford, UNITED KINGDOM, 2004.

[31]P. Jiang, X. Qian, X. Li, R. Yang, Three-dimensional anisotropic thermal conductivity tensor of single crystalline β-Ga_2O_3, Applied Physics Letters 113 (2018) 232105.

[32]A. Einstein, Über die von der molekularkinetischen Theorie der Wärme geforderte Bewegung von in ruhenden Flüssigkeiten suspendierten Teilchen, Annalen der Physik 322 (1905) 549–560.

[33]C. Kittel, Introduction to solid state, volume 162, John Wiley & Sons, 1966.

[34]L. Zhou, J. Huang, L. Cao, H. Ouyang, J. Wu, J. Liu, X. Wang, W. Hao, Synthesis of β-$Y_2Si_2O_7$ nanowires via a facile molten salt method and their thermal properties, Journal of Alloys and Compounds 699 (2017) 210–215.

[35]Z. Tian, L. Zheng, Z. Li, J. Li, J. Wang, Exploration of the low thermal conductivities of γ-$Y_2Si_2O_7$, β-$Y_2Si_2O_7$, β-$Yb_2Si_2O_7$, and β-$Lu_2Si_2O_7$ as novel environmental barrier coating candidates, Journal of the European Ceramic Society 36 (2016) 2813–2823.